



Preparation of g-C₃N₄/MoS₂ Composite Material and Its Visible Light Catalytic Performance

Yu Fan¹ · Yan-ning Yang^{1,2} · Chen Ding¹

Received: 15 June 2021 / Accepted: 3 September 2021 / Published online: 17 September 2021
© The Author(s), under exclusive licence to Springer Science+Business Media, LLC, part of Springer Nature 2021

Abstract

The g-C₃N₄ nanosheet was prepared by calcination method, the MoS₂ nanosheet was prepared by hydrothermal method. The g-C₃N₄/MoS₂ composites were prepared by ultrasonic composite in anhydrous ethanol. X-ray diffraction, scanning electron microscopy, transmission electron microscopy, X-ray photoelectron spectroscopy, ultraviolet–visible spectroscopy, and photoluminescence techniques were used to characterize the materials. The photocatalytic degradation of Rhodamine B (Rh B) by g-C₃N₄/MoS₂ composites with different mass ratios was investigated under visible light. The results show that a small amount of MoS₂ combined with g-C₃N₄ can significantly improve photocatalytic activity. The g-C₃N₄/MoS₂ composite with a mass ratio of 1:8 has the highest photocatalytic activity, and the degradation rate of Rh B increases from 50 to 99.6%. The main reason is that MoS₂ and g-C₃N₄ have a matching band structure. The separation rate of photogenerated electron–hole pairs is enhanced. So the g-C₃N₄/MoS₂ composite can improve the photocatalytic activity. Through the active material capture experiment, it is found that the main active material in the photocatalytic reaction process is holes, followed by superoxide radicals.

Keywords g-C₃N₄ nanosheet · MoS₂ nanosheet · g-C₃N₄/MoS₂ · Ultrasonic composite method · Visible light photocatalysis

1 Introduction

Printing and dyeing wastewater, as a kind of industrial wastewater, has a large discharge. According to statistics, every year the textile field of sewage discharge up to more than 900 million tons. Sewage discharge accounts for the sixth place in the total amount of industrial wastewater. Among them, the main component of textile industry wastewater is printing and dyeing wastewater. Therefore, the treatment of printing and dyeing wastewater mainly affects the treatment effect of textile wastewater. Printing and dyeing wastewater has many components, often containing slurry, auxiliaries and

fuels, high chroma, toxic and harmful, difficult to dispose. Direct discharge without treatment or improper treatment will seriously damage the ecological environment, threaten human health [1]. Traditional wastewater treatment methods include physical methods, advanced oxidation methods and biological methods. Photocatalytic technology can effectively decompose pollutants, is a green environmental protection treatment technology. It has the advantages of low energy consumption, easy operation, mild reaction conditions, and no secondary pollution [2]. Photocatalysis has attracted the attention of many researchers around the world since 1972 when the study of photocatalytic decomposition of water under ultraviolet light was reported on a single crystal TiO₂ electrode [3]. Wide-band gap semiconductor materials such as TiO₂ and ZnO have been extensively studied. But they react only in violet light and are not very efficient, which also hampers their use [4]. After decades of exploration and development, a large number of new semiconductor photocatalysts have been developed, such as metal oxide [5–7], metal sulfide [8, 9], silver halide [10, 11], silver phosphate [12, 13], layered bismuth oxyhalide [14, 15], and so on. New semiconductor photocatalysts can form a suitable bandwidth and use sunlight more efficiently.

✉ Yan-ning Yang
yangyanning@yau.edu.cn

Yu Fan
fanyu@yau.edu.cn

Chen Ding
dingchen@yau.edu.cn

¹ School of Physics and Electronic Information, Yan'an University, Yan'an 716000, China

² Shaanxi Key Laboratory of Intelligent Processing of Big Energy Data, Yan'an University, Yan'an 716000, China

In 2009, the team of Wang Xinchen [16] reported a kind of graphite-structured layered material for the first time, which was named graphite-phase carbon nitride ($g\text{-C}_3\text{N}_4$). It has a band gap of 2.7 eV. It shows a very strong ability of oxidation and photocatalytic decomposition of organic matter under visible light irradiation, which has been widely paid attention to by researchers [17]. However, the $g\text{-C}_3\text{N}_4$ has some shortcomings that make its photocatalytic effect poor. For example, its specific surface area is relatively small, and the photo-generated electron-holes are easy to recombine. These shortcomings make it unable to stand alone in the field of photocatalysis. For this reason, researchers have tried many methods to improve the photocatalytic activity of $g\text{-C}_3\text{N}_4$. Such as element doping [18, 19], precious metal deposition [20, 21], and semiconductor compounding [22, 23]. At present, two-dimensional (2D) materials can be used in many places, including the field of photocatalysis by their super large specific surface area and suitable forbidden band width. It is one of the frontiers of research. The 2D MoS_2 has attracted much attention due to its excellent properties, good electrical conductivity, and narrow band gap. In addition, because it has a unique energy band structure and good lattice matching, MoS_2 matches well with $g\text{-C}_3\text{N}_4$, which can effectively accelerate the transfer of electrons and holes [24]. Yan et al. [25] used the ball milling method to compound $g\text{-C}_3\text{N}_4$ with MoS_2 to disintegrate pollutants under visible light irradiation, which significantly improved the photocatalytic activity of semiconductor materials. Experimental facts have proved that the combination of $g\text{-C}_3\text{N}_4$ and MoS_2 can effectively promote the separation rate of photogenerated electron-hole pairs and improve the photocatalytic activity of $g\text{-C}_3\text{N}_4$. Ge et al. [26] loaded MoS_2 on the surface of $g\text{-C}_3\text{N}_4$ by the impregnation-calcination method, of which 0.5% (w/w) $\text{MoS}_2/g\text{-C}_3\text{N}_4$ photocatalytic hydrogen production activity was the best, which was about 11.3 times that of single $g\text{-C}_3\text{N}_4$. Li et al. [27] used the chemical ultrasonic method to prepare $g\text{-C}_3\text{N}_4/\text{MoS}_2$ composite catalyst successfully. The results showed that the addition of MoS_2 significantly improved the catalytic activity of $g\text{-C}_3\text{N}_4$ on Rh B and methylene blue under visible light. A large number of experiments show that MoS_2 is a good promoter.

In this paper, the $g\text{-C}_3\text{N}_4/\text{MoS}_2$ composite was prepared by a simple ultrasonic composite method. Compared with the paper listed in this paper, the main advantage is the preparation process is simple, easy to control, and as far as possible to avoid a series of uncontrollable factors. Its photocatalytic performance was verified by the degradation rate of Rh B under visible light irradiation. The crystal structure, microstructure and luminescence properties of the samples were characterized and analyzed by X-ray diffraction (XRD), scanning electron microscopy (SEM), transmission electron microscopy (TEM), X-ray photoelectron spectroscopy

(XPS), ultraviolet-visible spectroscopy (UV-Vis), and photoluminescence (PL). The mechanism of photocatalytic degradation was further discussed by capturing active substances.

2 Experiment

2.1 Preparation of Photocatalysts

Melamine, Rh B and ethanol were purchased from Sinopharm Chemical Reagent Co., Ltd (China). All reagents were at the analytical level. They were used without any further purification.

The $g\text{-C}_3\text{N}_4$ powder was prepared by thermal polymerization with melamine as raw material. 10 g of melamine powder was heated to 550 °C in a muffle furnace at the rate of 5 °C min^{-1} for 5 h. At the end of the reaction, the $g\text{-C}_3\text{N}_4$ powder was obtained by grinding.

MoS_2 nanosheets were prepared by the one-step hydrothermal method. Firstly, 0.28 mmol ammonium molybdate and 10 mmol thiourea were dissolved in 10 mL of deionized water. After magnetic stirring for 30 min, the solution was fully dissolved into a uniform solution by ultrasound for 30 min. Secondly, poured the solution into a 50 mL high-pressure reactor. After sealing, the reaction kettle was placed in the electric heating blast drying oven for hydrothermal reaction. The temperature was set at 200 °C, and the time was set at 10 h. Thirdly, the precipitate was cleaned repeatedly with deionized water and anhydrous ethanol. Finally, the precipitate was dried in a 60 °C oven for 10 h to collect black MoS_2 powder.

The $g\text{-C}_3\text{N}_4/\text{MoS}_2$ composite was prepared by a simple ultrasonic composite method. Firstly, 0.2 g $g\text{-C}_3\text{N}_4$ powder and 0.025 g MoS_2 powder were weighed and put into anhydrous ethanol. Secondly, the temperature was controlled at 40 °C, and ultrasonic concussion for 1.5 h [27]. Then, the solution was fully stirred in a blender for 36 h. Let the product stand and pour out the supernatant. Finally, the precipitate was put into the oven to dry at 80 °C for 10 h, and the $g\text{-C}_3\text{N}_4/\text{MoS}_2$ -8 composite was collected. The composite materials with mass ratios of 4:1, 6:1, 10:1, 12:1, and 14:1 were prepared according to the above scheme, which were, respectively called $g\text{-C}_3\text{N}_4/\text{MoS}_2$ -4, $g\text{-C}_3\text{N}_4/\text{MoS}_2$ -6, $g\text{-C}_3\text{N}_4/\text{MoS}_2$ -10, $g\text{-C}_3\text{N}_4/\text{MoS}_2$ -12, and $g\text{-C}_3\text{N}_4/\text{MoS}_2$ -14.

2.2 Sample Characterization

After preparing $g\text{-C}_3\text{N}_4$, MoS_2 , $g\text{-C}_3\text{N}_4/\text{MoS}_2$ nanomaterials. X-ray diffractometer (XRD, D/MAX2400, Rigaku Company, Japan, radiation source Cu $K\alpha$, tube voltage 40 kV, tube current 30 mA), scanning electron microscope (SEM, Hitachi TM3000, Japan), transmission electron microscope

(TEM, Fei Talos F200S Super-X spectrometer), X-ray photoelectron spectroscopy (XPS, Thermo Scientific, Escalab XI+ type XPS, Al target), UV–Vis spectrometer (UV–Vis, Shimadzu UV3600 Plus) and fluorescence spectroscopy (PL, Yokohama C9920-02G) were used to characterize the composition, morphology and light absorption properties of the materials.

2.3 Photocatalytic Tests

The photocatalytic performance of the samples was obtained by the photodegradation pathway of Rh B under visible light irradiation. A 500 W long arc xenon lamp with an AM 1.5 filter (100 mW cm^{-2}) was employed to simulate the visible light source. The 50 mg catalyst was dispersed in 50 mL of Rh B solution (the concentration of Rh B was 10 mg L^{-1}), and the photocatalyst was stirred with the Rh B solution in the dark for at least 30 min to ensure the adsorption–desorption equilibrium. In the process of photoreaction for 120 min, the concentration of pollutants was analyzed by UV–Vis spectrophotometer after extracting 4 mL of suspension each time and centrifugation. The wavelength range of Rh B was 450–600 nm.

3 Results and Discussion

3.1 XRD Analyses

Figure 1 shows the XRD pattern of $g\text{-C}_3\text{N}_4$, MoS_2 , and $g\text{-C}_3\text{N}_4/\text{MoS}_2\text{-8}$ complexes. For bulk phase pure MoS_2 , the diffraction peaks with 2θ angles of 14.4° , 32.7° , 35.8° and 58.4° matched the (002), (100), (102), and (110) crystal faces of hexagonal MoS_2 (JCPDS No. 37-1492) [28]. Pure $g\text{-C}_3\text{N}_4$ and $g\text{-C}_3\text{N}_4/\text{MoS}_2\text{-8}$ complexes have two broadened

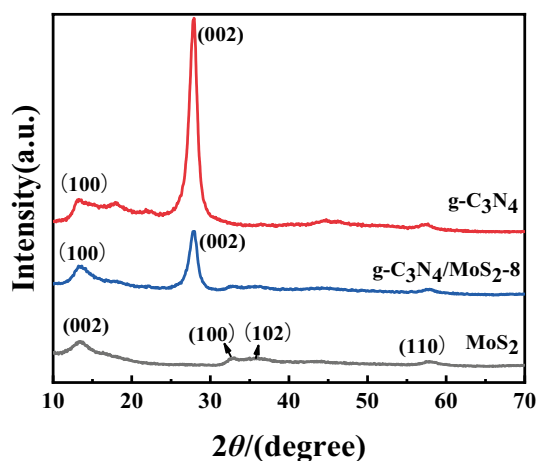


Fig. 1 XRD patterns of $g\text{-C}_3\text{N}_4$, $g\text{-C}_3\text{N}_4/\text{MoS}_2$ composite, and MoS_2

diffraction peaks at 2θ angles of 13.0° and 27.6° , which are characteristic peaks of $g\text{-C}_3\text{N}_4$. They correspond to its (100) and (002) crystal faces [29]. The (002) diffraction peak of the $g\text{-C}_3\text{N}_4/\text{MoS}_2\text{-8}$ composite is weaker than $g\text{-C}_3\text{N}_4$. This indicates that MoS_2 does not change the lattice of $g\text{-C}_3\text{N}_4$. There is no obvious diffraction peak of MoS_2 in $g\text{-C}_3\text{N}_4/\text{MoS}_2\text{-8}$, which may be due to the low content of MoS_2 . Fig. S1 shows the XRD patterns of all samples. All the complexes have the characteristic peak of $g\text{-C}_3\text{N}_4$, and the diffraction peak of the $g\text{-C}_3\text{N}_4/\text{MoS}_2\text{-8}$ complex is the weakest at 27.6° . It indicates that the crystallinity of $g\text{-C}_3\text{N}_4$ is low, and MoS_2 has been well compounded with $g\text{-C}_3\text{N}_4$.

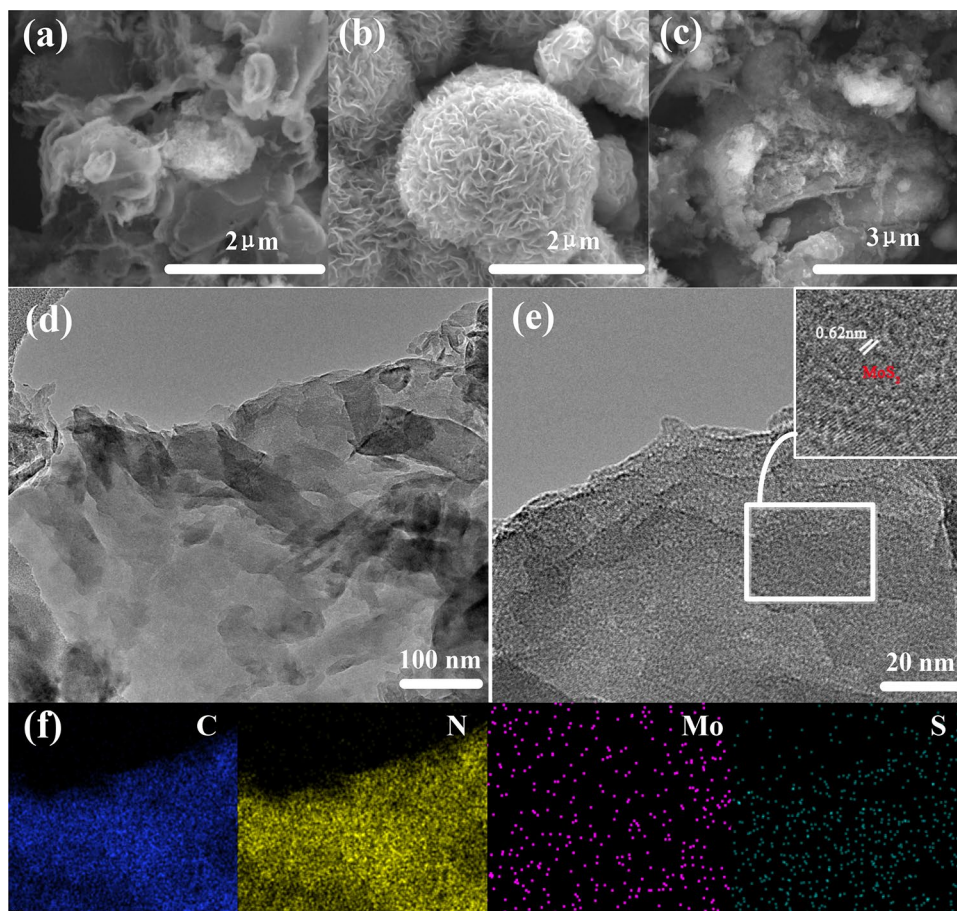
3.2 SEM and TEM Analyses

The microstructure of the $g\text{-C}_3\text{N}_4$, MoS_2 , and $g\text{-C}_3\text{N}_4/\text{MoS}_2\text{-8}$ were examined by SEM and transmission electron microscopy. Figure 2a shows the scanning electron microscope image of the $g\text{-C}_3\text{N}_4$. The aggregation structure of unevenly curved nanosheets with some pores, which may be caused by the release of gas during high temperature aggregation. Figure 2b shows the SEM figure of the MoS_2 , from which it can be seen that the nano-flake MoS_2 is curved and curled up into a spherical shape. Figure 2c shows the SEM image of the $g\text{-C}_3\text{N}_4/\text{MoS}_2\text{-8}$. It can be seen from the figure that the relatively flat $g\text{-C}_3\text{N}_4$ nanosheets and the original flower-like MoS_2 nanosheets disappear and become porous and small-area lamellate structures. Particularly, the phenomenon of clustering is obvious. The morphology of the $g\text{-C}_3\text{N}_4/\text{MoS}_2$ composites was further studied by TEM and HRTEM images. Figure 2d shows there are two kinds of nanosheets superposed together. Figure 2e shows 0.62 nm lattice spacing appears in the composite material, which can be attributed to the (002) crystal plane of MoS_2 [30]. The existence of MoS_2 is also proved. The test of sample element mapping was carried out on the composite material, as shown in Fig. 2f, and the elements of carbon, nitrogen, molybdenum and sulfur were evenly distributed in the sheet sample. These results show that MoS_2 recombines with $g\text{-C}_3\text{N}_4$, indicating the formation of $g\text{-C}_3\text{N}_4/\text{MoS}_2$ heterojunction.

3.3 XPS Analyses

The chemical compositions and states of C, N, Mo, and S elements in $g\text{-C}_3\text{N}_4/\text{MoS}_2\text{-8}$ heterostructures have been studied by XPS. Figure 3a shows that in the C 1s spectrum, there are two peaks at about 284.8 eV and 285.9 eV. The binding energy peak at 284.8 eV corresponds to the C–C group. The peak at 285.9 eV corresponds to the N–C=N group of $g\text{-C}_3\text{N}_4$. Figure 3b shows the N 1s spectrum can be fitted to three peaks at 395.3 eV, 397 eV and 401.2 eV, which can be attributed to C–N–C, N–(C)₃ and N–H groups [31]. In

Fig. 2 SEM diagram of g-C₃N₄ (a), MoS₂ (b), g-C₃N₄/MoS₂ (c) composite; TEM images of g-C₃N₄/MoS₂-8 composite (d); HRTEM images of g-C₃N₄/MoS₂-8 composite (e); g-C₃N₄/MoS₂-8 complex element mapping (f), C element, N element, Mo element, S element



the Mo 3*d* spectrum, three peaks can be observed, which are 224.9 eV, 228.32 eV, and 231.9 eV. It is shown that the Mo element in g-C₃N₄/MoS₂-8 mainly exists in the form of Mo⁴⁺. Figure 3d shows the two major peaks at 157.8 eV and 159 eV. The peak of 157.8 eV is attributed to S 2*p*_{3/2} and 159 eV is attributed to S 2*p*_{1/2}. They are consistent with S²⁻ in MoS₂. The results show that MoS₂ nanosheets are successfully combined with g-C₃N₄ nanosheets.

3.4 UV–Vis Analyses

Figure 4 shows the UV–Vis diffuse reflectance spectra of the g-C₃N₄ and g-C₃N₄/MoS₂-8 nanosheets. The g-C₃N₄ sample shows the absorption of up to 460 nm in the ultraviolet to visible range, due to the small band gap of g-C₃N₄. To compare with g-C₃N₄, the absorption wavelength of g-C₃N₄/MoS₂-8 composites reaches 475 nm. According to the formula:

$$Eg = 1240/\lambda g$$

λg is the semiconductor absorption band boundary value, the band gap of g-C₃N₄ is about 2.70 eV. The band gap of g-C₃N₄/MoS₂-8 is about 2.61 eV. The results show that the

MoS₂ is successfully combined with g-C₃N₄. The band gap of the photocatalyst decreases with the introduction of MoS₂. Because of the small band gap of MoS₂ and its ability to absorb near-infrared light. Fig. S7 shows the absorption of g-C₃N₄/MoS₂ complexes that in the whole visible region was enhanced. And with the increase of MoS₂ content, the absorption intensity also increases. Therefore, g-C₃N₄/MoS₂ heterojunction can capture more visible light and enhance the catalytic activity.

3.5 PL Analyses

The separation and recombination of photogenerated electron–hole pairs are very important for the performance of catalysts. Figure 5 shows the PL spectra of the sample. In general, the optical properties of photocatalysts in the visible region can be interpreted as the composition of photogenerated electrons and holes. Figure 5 shows that monomer g-C₃N₄ has a strong fluorescence emission peak at about 470 nm. The results show that in g-C₃N₄ nanomaterials, the electron–hole pair generated by light is easy to combine, which is not good for its photocatalytic performance. The PL spectra of g-C₃N₄/MoS₂-8 composite photocatalyst decreased obviously. And the PL intensity of g-C₃N₄/

Fig. 3 XPS spectra of g-C₃N₄/MoS₂-8; deconvoluted peaks for **a** C 1s, **b** N 1s, **c** Mo 3d, **d** S 2p

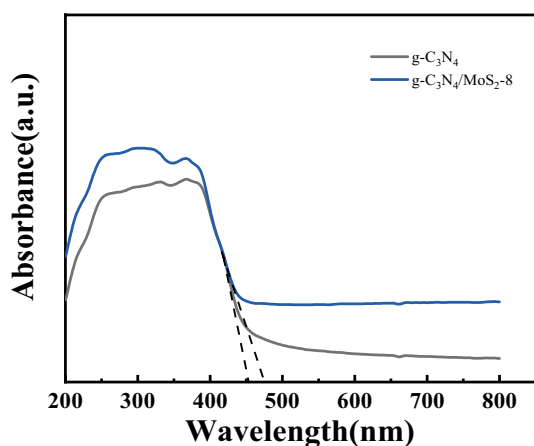
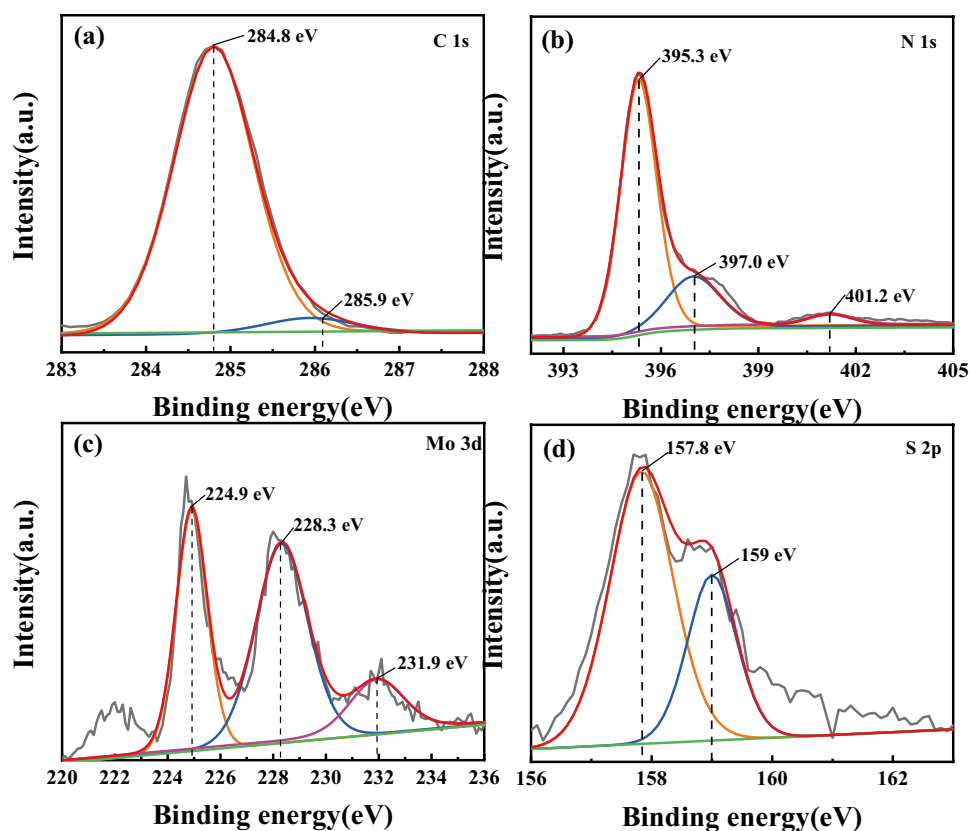


Fig. 4 UV-Vis spectra of g-C₃N₄, MoS₂, and g-C₃N₄/MoS₂-8 composite

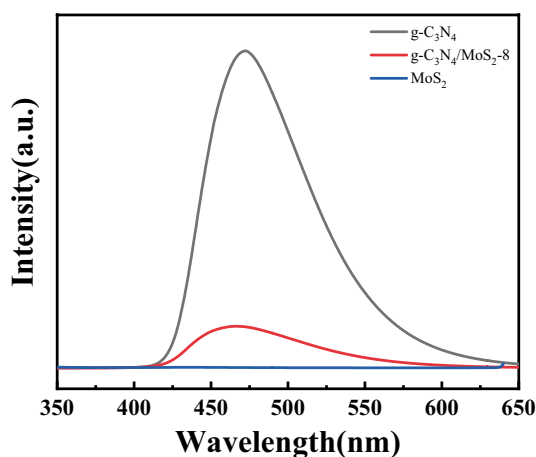


Fig. 5 PL spectra of g-C₃N₄, MoS₂, and g-C₃N₄/MoS₂-8 composite

MoS₂-8 is the lowest among all the composites (as shown in Fig. S8). This could inhibit the compound efficiency of photogenerated electrons and holes and improve the activity of photocatalyst.

3.6 Photocatalytic Activity Analyses

The photocatalytic degradation of g-C₃N₄ and MoS₂ complexes with different mass ratios was studied under visible light irradiation using Rh B as a simulated pollutant. Figure 6 shows the curve of the photocatalytic degradation rate of different photocatalysts over time. The result shows

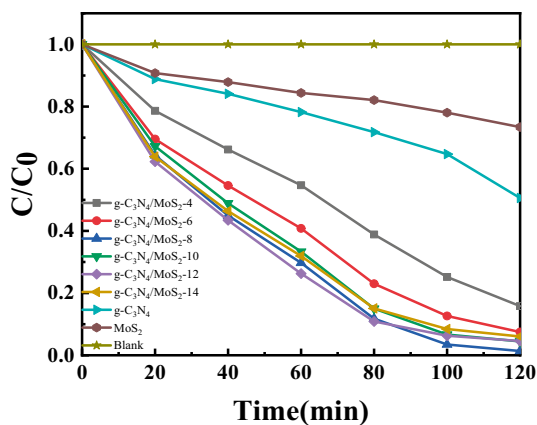


Fig. 6 Photocatalytic degradation curve of Rh B solution by different samples

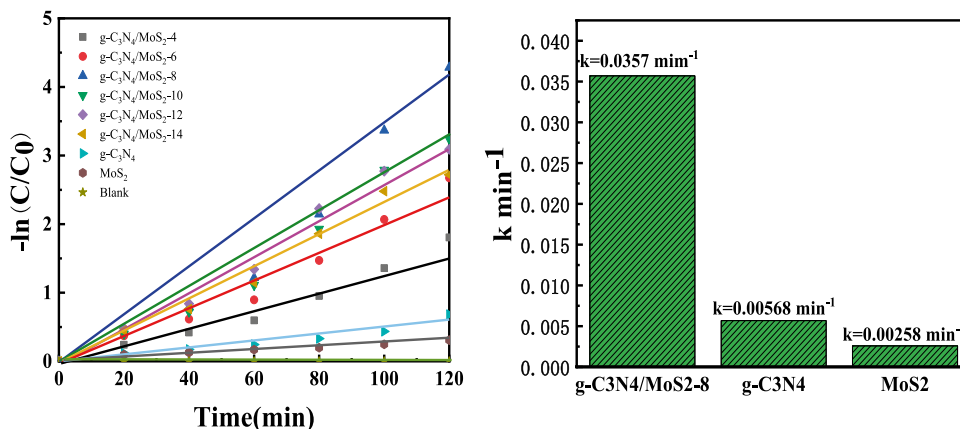
that the g-C₃N₄/MoS₂-8 composite had the best degradation effect. The photodegradation rate of Rh B reached 99.6%. The degradation rate of Rh B by pure g-C₃N₄ was 50% after 120 min of light exposure. Therefore, the degradation effect of Rh B by catalyst combined with MoS₂ was nearly two times that of pure catalyst.

For low concentrations of organic pollutants, the kinetic behavior of degradation reaction can be studied by the following equation:

$$\ln(C/C_0) = kt$$

C is the concentration of pollutants degraded by photocatalyst (mg L⁻¹), C₀ is the adsorption equilibrium concentration of pollutants before radiation (mg L⁻¹), t is the reaction time (min), and k is the kinetic constant (min⁻¹). Figure 7 shows the Kinetic constant k of different samples. The k values of g-C₃N₄/MoS₂-8 composites, g-C₃N₄, and MoS₂ photocatalysts were calculated as 0.0357 min⁻¹, 0.00568 min⁻¹, and 0.00258 min⁻¹. The results show that the degradation rate constant of the composite photocatalyst was 6.3 times of the

Fig. 7 Photocatalytic reaction rate constants of different samples



original g-C₃N₄ photocatalyst and 13.8 times of the MoS₂ photocatalyst. Therefore, the photocatalytic activity of the composite material for Rh B degradation was significantly improved.

In order to study the photocatalytic stability of g-C₃N₄/MoS₂-8 photocatalyst. The g-C₃N₄/MoS₂-8 powder was cycled five times under the same reaction conditions. Figure 8 shows a relatively stable photocatalytic performance. After five cycles, g-C₃N₄/MoS₂-8 photocatalyst still maintained a relatively high photocatalytic performance for the degradation of Rh B, and the photodegradation rate was 97% after 120 min of illumination. The precipitation and transfer processes may be the main reasons for the degradation of photocatalytic performance. Therefore, g-C₃N₄/MoS₂-8 photocatalyst showed high photocatalytic activity and excellent recoverability for the degradation of organic pollutants under visible light irradiation. This showed great potential for future practical applications.

There are a series of photoinduced active substances such as superoxide radicals (·O₂⁻), hydroxyl radicals (·OH) and holes (h⁺) in the process of photocatalytic reaction. They

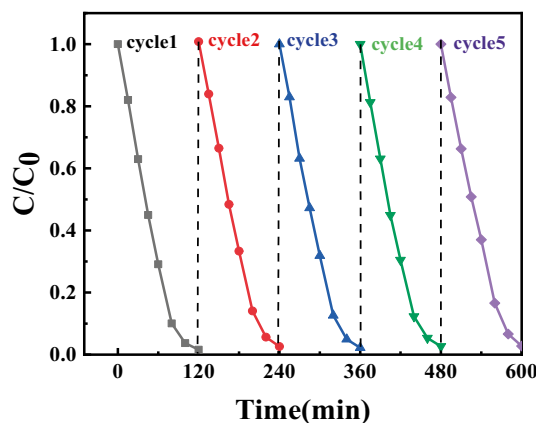


Fig. 8 Cyclic degradation curve of g-C₃N₄/MoS₂-8 composite

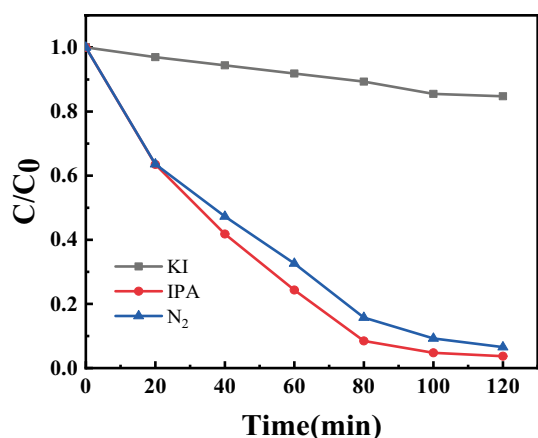


Fig. 9 The effect of the trapping agent on the photocatalytic activity

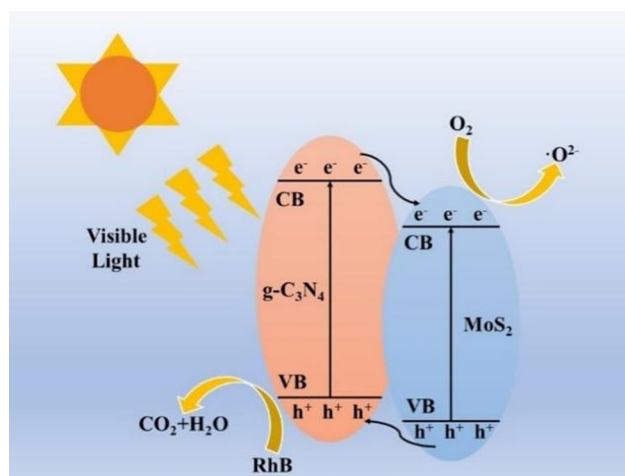


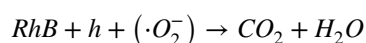
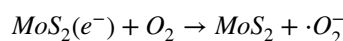
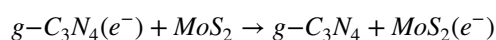
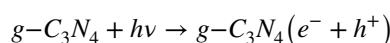
Fig. 10 Photocatalytic enhancement mechanism diagram of $g\text{-C}_3\text{N}_4/\text{MoS}_2\text{-8}$ composite

will directly participate in the photocatalytic process of Rh B under visible light irradiation. In order to elucidate the role of different substances in the redox reaction, different scavengers were added to the photocatalyst to carry out the reaction. N_2 was added to remove the $\cdot\text{O}_2^-$, isopropanol (IPA) to remove the $\cdot\text{OH}$, and KI to remove the h^+ . The original $g\text{-C}_3\text{N}_4/\text{MoS}_2\text{-8}$ photocatalyst was fed with homogeneous N_2 , 0.5 mmol KI and 0.5 mmol IPA. Their degradation effect on Rh B was measured under visible light irradiation. Figure 9 shows that only 15% of Rh B is degraded by adding KI to the photocatalyst, 93% of Rh B is degraded by adding N_2 to the photocatalyst, and 97% of Rh B is degraded by adding isopropanol. It can be seen that all three substances participate in the photocatalytic reaction. But the main role is the h^+ followed by the $\cdot\text{O}_2^-$.

Figure 10 illustrates the mechanism of improving the photocatalytic activity of the $g\text{-C}_3\text{N}_4/\text{MoS}_2$ composite. Under illumination, $g\text{-C}_3\text{N}_4$ absorbs visible light and is excited to produce photogenerated electron–hole pairs. The photogenerated electrons transition from the valence band (VB) to the conduction band (CB) and leave holes in the valence band. According to the theoretical values, the conduction band potentials (E_{CB}) of $g\text{-C}_3\text{N}_4$ is about -1.22 eV and MoS_2 is about -0.12 eV. The band gaps between them are about 2.88 eV and 1.90 eV. Then according to:

$$E_{\text{VB}} = E_{\text{CB}} + E_g$$

it can be seen that their valence band potentials (E_{VB}) are about 1.66 and 1.78 eV [32]. They have a matching band structure. When $g\text{-C}_3\text{N}_4$ and MoS_2 are combined. Since the CB potential of $g\text{-C}_3\text{N}_4$ is more negative than MoS_2 . The photoinduced electrons in the CB of $g\text{-C}_3\text{N}_4$ can be easily transferred to the CB of MoS_2 through the interface. At the same time, because the VB position of $g\text{-C}_3\text{N}_4$ is more negative than MoS_2 . The holes in the VB of MoS_2 move to the VB position of $g\text{-C}_3\text{N}_4$ in a similar manner, facilitating the separation of the photogenerated electrons from the holes. Electrons are collected in CB of MoS_2 and the holes are collected in VB of $g\text{-C}_3\text{N}_4$. Therefore, the probability of electron–hole recombination is hindered. It can reduce the probability of photo-generated carrier recombination and prolongs the life of the photo-generated carrier. Therefore, the photocatalytic activity is improved. According to the report, the redox potential of $\text{OH}^-/\cdot\text{OH}$ is about 2.27 eV [33]. Therefore, the holes generated in the VB cannot directly oxidize the OH^- or water molecules adsorbed on the surface of the catalyst to $\cdot\text{OH}$ directly. But directly oxidize the organic matter in the form of holes. So one of the main active species in the photocatalytic experiment is the hole. On the other hand, the photogenerated electrons transferred to MoS_2 have higher reducing power. The redox potential of $\text{O}_2/\cdot\text{O}_2^-$ is about 0.33 eV [34]. It can react with O_2 adsorbed on the catalyst surface to generate $\cdot\text{O}_2^-$. So the other major reactive agent is the $\cdot\text{O}_2^-$. And get the following equation:



Therefore, through the above analysis, it can be expected that the photodegradation activity of the photocatalyst can be effectively improved by forming the g-C₃N₄/MoS₂ heterojunction.

4 Conclusion

The g-C₃N₄ nanosheets and MoS₂ nanosheets were synthesized by thermal polymerization and hydrothermal method. Then ultrasonically composited with g-C₃N₄. The g-C₃N₄/MoS₂ composite material was obtained simply. The experiment of photocatalytic degradation of Rh B shows that under the irradiation of visible light, the composite of a small amount of MoS₂ significantly improves the photocatalytic activity of g-C₃N₄. The best photocatalytic activity was that the g-C₃N₄/MoS₂ composite with a mass ratio of 8:1. The degradation effect can reach 99.6% after 120 min of illumination. The active matter capture experiment shows that the main active matter in the photocatalytic reaction process is holes, followed by superoxide radicals. UV–Vis diffuse reflectance shows that the band gap of the composite material is reduced, thereby the photocatalytic activity has been enhanced. In addition, the g-C₃N₄/MoS₂ composite also shows good light stability. The above results show that the material has good application prospects in the photocatalytic treatment of organic pollutants.

Supplementary Information The online version contains supplementary material available at <https://doi.org/10.1007/s10904-021-02099-7>.

Acknowledgements This study was funded by the National Natural Science Foundation of China (61664008), Yan'an Science and Technology Planning Project (2019ZCNZ-001); Yan'an University Industry-University-Research Cooperation Project (CXY201902); Research Fund for key Laboratories jointly built by provinces and cities of Shaanxi Province for Intelligent Processing of Big Data (IPBED11, IPBED16); Graduate Education Reform Program of Yan'an University (YDYJG2019018).

References

1. S. Palanivel, A. Mani, P. Thayumanavan, Utilization of agro-industrial waste *Jatropha curcas* pods as an activated carbon for the adsorption of reactive dye Remazol Brilliant Blue R (RBBR). *J. Clean. Prod.* **22**(1), 67–75 (2012)
2. N. Li, H. Gao, X. Wang, S.J. Zhao, D. Lv, G.Q. Yang, X.Y. Gao, H.K. Fan, Y.Q. Gao, L. Ge, Novel indirect Z-scheme g-C₃N₄/Bi₂MoO₆/Bi hollow microsphere heterojunctions with SPR-promoted visible absorption and highly enhanced photocatalytic performance. *Chin. J. Catal.* **41**(03), 426–434 (2020)
3. B.X. Zhang, S.X. Cao, M.Q. Du, X.Z. Ye, Y. Wang, J.F. Ye, Titanium dioxide (TiO₂) mesocrystals: synthesis, growth mechanisms and photocatalytic properties. *Catalysts* **9**(1), 91 (2019)
4. H. Park, Y. Park, W. Kim, W. Choi, Surface modification of TiO₂ photocatalyst for environmental applications (review). *J. Photochem. Photobiol. C* **15**(1), 1–20 (2013)
5. B.A. Carlos J., G. Javier, A. Raul, L. Marta, B.P. Bruno, H. Jose L., Anisotropic Au-ZnO photocatalyst for the visible-light expanded oxidation of n-hexane. *Cataly Today* **362**, 97–103 (2021)
6. J.A. Quek, J.C. Sin, S.M. Lam, A.R. Mohamed, H.H. Zeng, Bioinspired green synthesis of ZnO structures with enhanced visible light photocatalytic activity. *J. Mater. Sci. Mater. Electron.* **31**(2), 1144–1158 (2020)
7. S.Q. Wu, H.Y. Hu, Y. Lin, J.L. Zhang, Y.H. Hu, Visible light photocatalytic degradation of tetracycline over TiO₂. *Chem. Eng. J.* **382**, 122842 (2020)
8. Y.P. Xie, Z.B. Yu, G. Liu, X.L. Ma, H.M. Cheng, Cds-mesoporous ZnS core-shell particles for efficient and stable photocatalytic hydrogen evolution under visible light. *Energy Environ. Sci.* **7**(6), 1895–1901 (2014)
9. J.H. Liu, G.F. Huang, W.Q. Huang, H. Miao, B.X. Zhou, Morphology-controlled SnS₂ nanostructures synthesized by refluxing method with high photocatalytic activity. *Mater. Lett.* **161**(1), 480–483 (2015)
10. A.D. Di, Y. Wang, G. Chen, Dendritic hierarchical AgCl prepared in the interface of gas-solid as the precursors of the visible-light plasmonic photocatalysts of Ag–AgCl. *Funct. Mater. Lett.* **11**(1), 1850006 (2018)
11. Y.Q. Yang, R.X. Liu, G.K. Zhang, L.Z. Gao, W.K. Zhang, Preparation and photocatalytic properties of visible light driven Ag–AgCl–TiO₂/palygorskite composite. *J. Alloys Compd.* **657**, 801–808 (2016)
12. W.K. Ji, Z.B. Rui, H.B. Ji, Z-scheme Ag₃PO₄/Ag/SrTiO₃ heterojunction for visible-light induced photothermal synergistic VOCs degradation with enhanced performance. *Ind. Eng. Chem. Res.* **58**(31), 13950–13959 (2019)
13. A. Tab, B. Bellal, C. Belabed, M. Dahmane, M. Trari, Visible light assisted photocatalytic degradation and mineralization of Rhodamine B in aqueous solution by Ag₃PO₄. *Optik* **214**, 164858 (2020)
14. X.Y. Gao, W. Peng, G.B. Tang, Q. Guo, Y.M. Luo, Highly efficient and visible-light-driven BiOCl for photocatalytic degradation of carbamazepine. *J. Alloys Compd.* **757**, 455–465 (2018)
15. Z.L. Liu, F.Y. Lv, Y. Xiao, B. Chen, J. Qiu, W.Z. Guo, Y. Wen, Z. Li, Z.S. Liu, Mor-phologycontrollable synthesis of BiOBr architectures and their visible light photocatalytic activities. *Mater. Technol.* **34**(11), 683–688 (2019)
16. X.C. Wang, K. Maeda, A. Thomas, K. Takanebe, G. Xin, J.M. Carlsson, K. Domen, M. Antonietti, A metal-free polymeric photocatalyst for hydrogen production from water under visible light. *Nat. Mater.* **8**(1), 76–80 (2009)
17. J. Li, E.Z. Liu, Y.N. Ma, X.Y. Hu, J. Wan, L. Sun, J. Fan, Synthesis of MoS₂/g-C₃N₄ nanosheets as 2D heterojunction photocatalysts with enhanced visible light activity. *Appl. Surf. Sci.* **364**, 694–702 (2016)
18. M. Zhang, X.J. Bai, D. Liu, J. Wang, Y.F. Zhu, Enhanced catalytic activity of potassium-doped graphitic carbon nitride induced by lower valence position. *Appl. Catal. B* **164**, 77–81 (2015)
19. D.D. Xu, X.N. Li, J. Liu, L.H. Huang, Synthesis and photocatalytic performance of europium-doped graphitic carbon nitride. *J. Rare Earths* **31**(11), 1085–1091 (2013)
20. N.Y. Cheng, J.Q. Tian, Q. Liu, C.J. Ge, A.H. Qusti, A.M. Asiri, A.O. Al-Youbi, X.P. Sun, Au-nanoparticle-loaded graphitic carbon nitride nanosheets: green photocatalytic synthesis and application toward the degradation of organic pollutants. *ACS Appl. Mater. Interfaces* **5**(15), 6815–6819 (2013)

21. Y.L. Meng, J. Shen, D. Chen, G. Xin, Photodegradation performance of methylene blue aqueous solution on Ag/g-C₃N₄ catalyst. *Rare Met.* **30**(s1), 276–279 (2011)
22. Y.G. Wang, Y.Z. Wang, Y.T. Chen, C.C. Yin, Y.H. Zuo, L.F. Cui, Synthesis of Ti-doped graphitic carbon nitride with improved photocatalytic activity under visible light. *Mater. Lett.* **139**, 70–72 (2015)
23. J.L. Chen, Z.H. Hong, Y.L. Chen, B.Z. Lin, B.F. Gao, One-step synthesis of sulfur-doped and nitrogen-deficient g-C₃N₄ photocatalyst for enhanced hydrogen evolution under visible light. *Mater. Lett.* **145**, 129–132 (2015)
24. M.L. Li, L.X. Zhang, X.Q. Fan, M.Y. Wu, Y.Y. Du, M. Wang, Q.L. Kong, L.L. Zhan-g, J.L. Shi, Dual synergetic effects in MoS₂/pyridine-modified g-C₃N₄ composite for highly active and stable photocatalytic hydrogen evolution under visible light. *Appl. Catal. B* **190**, 36–43 (2016)
25. X. Yan, Q. Gao, X. Hui, C. Yan, T. Ai, Z. Wang, G. Sun, X. Su, P. Zhao, Fabrication of g-C₃N₄/MoS₂ nanosheet heterojunction by facile ball milling method and its visible light photocatalytic performance. *Rare Metal Mater. Eng.* **47**(10), 3015–3020 (2018)
26. L. Ge, C.C. Han, X.L. Xiao, L.L. Guo, Synthesis and characterization of composite visible light active photocatalysts MoS₂-C₃N₄ with enhanced hydrogen evolution activity. *Int. J. Hydrogen Energy* **38**(17), 6960–6969 (2013)
27. Q. Li, N. Zhang, Y. Yang, G.Z. Wang, N.H.L. Dickon, High efficiency photocatalysis for pollutant degradation with MoS₂/C₃N₄ heterostructures. *Langmuir* **30**(29), 8965–8972 (2014)
28. W.J. Zhou, Z.Y. Yin, Y.P. Du, X. Huang, Z.Y. Zeng, Z.X. Fan, H. Liu, J.Y. Wang, H. Zhang, Synthesis of few-layer MoS₂ nanosheet-coated TiO₂ nanobelt heterostructures for enhanced photocatalytic activities. *Small* **9**(1), 140–147 (2013)
29. Y.N. Ma, E.Z. Liu, X.Y. Hu, C.N. Tang, J. Wan, J. Li, J. Fan, A simple process to prepare few-layer g-C₃N₄ nanosheets with enhanced photocatalytic activities. *Appl. Surf. Sci.* **358**(Part A), 246–251 (2015)
30. L. Guo, Z. Yang, K. Marcus, Z. Li, B. Luo, L. Zhou, X. Wang, Y. Du, Y. Yang, MoS₂/TiO₂ heterostructures as nonmetal plasmonic photocatalysts for highly efficient hydrogen evolution. *Energy Environ. Sci.* **11**(1), 106–114 (2017)
31. X.F. Yang, Z.P. Chen, J.S. Xu, H. Tang, K.M. Chen, Y. Jiang, Tuning the morphology of g-C₃N₄ for improvement of Z-scheme photocatalytic water oxidation. *ACS Appl. Mater. Interfaces* **7**(28), 15285–15293 (2015)
32. M.J. Lucero, J.K. Ellis, G.E. Scuseria, The indirect to direct band gap transition in multilayered MoS₂ as predicted by screened hybrid density functional theory. *Appl. Phys. Lett.* **99**(26), 261908 (2011)
33. X. Chen, P.F. Tan, B.H. Zhou, H.G. Dong, J. Pan, X. Xiong, A green and facile strategy for preparation of novel and stable Cr-doped SrTiO₃/g-C₃N₄ hybrid nanocomposites with enhanced visible light photocatalytic activity. *J. Alloys Compd.* **647**(15), 456–462 (2015)
34. H.L. Lv, G.B. Ji, Z.H. Yang, Y.S. Liu, X.M. Zhang, W. Liu, H.Q. Zhang, Enhancement photocatalytic activity of the graphite-like C₃N₄ coated hollow pencil-like ZnO. *J. Colloid Interface Sci.* **450**, 381–387 (2015)

Publisher's Note Springer Nature remains neutral with regard to jurisdictional claims in published maps and institutional affiliations.